Convexification of Semi-activity Constraints Applied to Minimum-time Optimal Control for Vehicles with Semi-active Limited-slip Differential

Tadeas Sedlacek[1,2][a], Dirk Odenthal[1][b] and Dirk Wollherr[2][c]
[1]*BMW M GmbH, Daimlerstr. 19, 85748 Garching near Munich, Germany*
[2]*Chair of Automatic Control Engineering, Department of Electrical and Computer Engineering, Technical University of Munich, Theresienstr. 90, 80333 Munich, Germany*

Keywords: Minimum Lap Time, Semi-active Limited-slip Differential, Convexification, Time Optimal Control, Hermite-Simpson Collocation, Vehicle System Dynamics.

Abstract: Semi-active actuators provide a good compromise between low energy consumption and high performance. Thus, they are deployed in many engineering applications, often combined with other actuators into complex systems requiring an integrated control concept for optimal performance. Optimal control can be used to objectively evaluate the performance of such systems as well as to deduce optimal control input trajectories and optimal passive system designs. We present a novel approach which enables considering a broad class of semi-active actuators in optimal control problems via convex sets. This procedure is exemplarily depicted for semi-active limited-slip differentials which are used in automotive applications for lateral torque distribution. The performance benefit gained by installing a semi-active limited-slip differential at the rear axle of a vehicle is objectively quantified by numerically computing time-optimal trajectories on a racetrack via direct optimal control with Hermite-Simpson collocation. Although the overall problem remains nonconvex for this particular application, this procedure is a first step towards a fully convex implementation. By iteratively increasing the upper boundary for the differential torque in multiple optimisations, we identify the smallest upper differential torque boundary for optimal laps and determine the lap time sensitivity regarding this limit.

SCIENCE AND TECHNOLOGY PUBLICATIONS

1 INTRODUCTION

Semi-active actuators are used in many engineering applications since they provide a good compromise between low energy consumption and high performance (Savaresi et al., 2010). For instance, semi-active dampers are deployed in automotive suspension systems (Savaresi et al., 2010), in landing gears for aircrafts (Krüger, 2000), in robotics to improve running (Kim et al., 2018), in architectural and bio-mechanical structures and many more (Poussot-Vassal et al., 2010). Further examples for semi-active actuators in the field of automotive engineering are semi-active limited-slip differentials (SLDs) for lateral torque distribution, semi-active transfer cases for longitudinal torque allocation and airsprings for an adjustable stiffness (Cheli et al., 2006; Savaresi et al., 2010). This paper focusses on SLDs which enable transferring torque from the faster spinning wheel to the slower one. Since only the amount of torque transferred by the differential can be controlled, whereas the direction of the torque transfer is dictated by the wheel speed difference, these actuators represent semi-active components. SLDs improve the cornering performance of vehicles by enhancing acceleration potential and yaw agility (Cheli et al., 2006). Lap times on racetracks can be used as a metric to objectively evaluate these benefits in vehicle performance. The time-optimal input trajectories for the multiple actuators of a vehicle under consideration of actuator limitations and track boundaries can be deduced by optimal control methods.

Optimal control has been successfully applied to compute input trajectories for limited-slip differentials (LDs) aiming at minimum lap times on racetracks. Passive LDs have been analysed via optimal control methods in (Kelly, 2008; Perantoni and Limebeer, 2014; Limebeer et al., 2014; Limebeer and Perantoni, 2015; Tremlett et al., 2015), whereas optimal trajectories for SLDs have been identified in (Tremlett and Limebeer, 2016). All approaches

[a] https://orcid.org/0000-0002-6191-6173
[b] https://orcid.org/0000-0002-6651-8369
[c] https://orcid.org/0000-0003-2810-6790

Sedlacek, T., Odenthal, D. and Wollherr, D.
Convexification of Semi-activity Constraints Applied to Minimum-time Optimal Control for Vehicles with Semi-active Limited-slip Differential.
DOI: 10.5220/0009593600150025
In *Proceedings of the 17th International Conference on Informatics in Control, Automation and Robotics (ICINCO 2020)*, pages 15-25
ISBN: 978-989-758-442-8
Copyright © 2020 by SCITEPRESS – Science and Technology Publications, Lda. All rights reserved

have in common that the torque transmitted by the differential is depicted as a function of the wheel speed difference. In the simplest form, the wheel speed difference is scaled by a factor which is either fixed for passive LDs or represents a system input when SLDs are considered. The computed differential torque has been either inserted into the differential equations of the system (Kelly, 2008) or has been considered by equality constraints (Perantoni and Limebeer, 2014; Limebeer et al., 2014; Limebeer and Perantoni, 2015; Tremlett et al., 2015; Tremlett and Limebeer, 2016). Except for (Kelly, 2008; Tremlett et al., 2015), only quasi steady-state wheel dynamics have been considered for the wheel speed to simplify the optimisation problem.

In this paper, we revisit the optimal control problem (OCP) introduced in (Sedlacek et al., 2020b) and augment the baseline vehicle model by a SLD at the rear axle. Since the rotational wheel speeds are decisive variables for LDs, the corresponding differential equations are included into the system dynamics. Furthermore, we consider maximum differential torque boundaries for the SLD. Formulating the contemplated OCP via the methods used in previous papers would result in either quadratic equality constraints or nonconvex sets, both prohibiting a fully convex OCP beforehand (Boyd and Vandenberghe, 2004). Using the SLD as an example, we present a novel OCP-modelling approach for semi-active components with convex subsets in the two quadrants dictated by the passivity constraint (Savaresi et al., 2010). The nonconvex set is transformed into two convex ones by separate consideration of positive and negative control inputs. The downside of this method is the requirement of an extra input and a generally higher number of constraints. However, this convexification procedure is a first step towards a fully convex OCP for such vehicles. The correctness of the approach is confirmed by analysing the resulting optimal trajectories. Finally, we identify the smallest upper differential torque boundary for optimal laps on a specified racetrack and determine the lap time sensitivity regarding this limit.

The remainder of this paper is organised as follows. The considered track model and vehicle model are presented in section 2. The OCP aiming at computing trajectories for minimum lap time is formulated in section 3 and its solution is discussed in section 4. Section 5 concludes the paper and gives an outlook for future work. The appendix contains further modelling details and parameter values.

2 VEHICLE MODEL

A nonlinear two-track vehicle model in combination with a flat track model is used to investigate optimal lap trajectories for the Nuerburg-ring Grand-Prix course. The topview of the vehicle model with respect to the racetrack is illustrated in figure 1. We introduce the index $k \in \mathbb{K} := \{1,2,3,4\}$ to distinguish the individual wheels and make use of several coordinate frames. Vectors given in the body coordinate frame, which is coupled with the centre of gravity (COG) of the vehicle and rotated by the yaw angle ψ around the z-axis of the inertial frame, are marked with the superscript b. Analogously, the wheel coordinate frame w is the result of a rotation by the front steering angle δ_f. Calligraphic symbols denote vector components given in the corresponding wheel coordinate frame.

Drive torque generated by a combustion engine is transmitted via a gear box and a SLD to the rear wheels. The wheel-based engine torque T_e considers gear ratios and constant efficiencies of transmission and SLD. The drive torque transferred laterally by the SLD is denoted with T_d. The front wheels are mounted on individual axles and are thus decoupled. Wheel-independent brake torques $T_{br,k}$ facilitate a longitudinal and lateral brake torque allocation. We assume that the differential only transfers drive torque and brake torque is solely allocated via the braking system. This yields the individual wheel torques

$$\begin{bmatrix} T_1 \\ T_2 \\ T_3 \\ T_4 \end{bmatrix} = \begin{bmatrix} -T_{br,1} \\ -T_{br,2} \\ \frac{1}{2}(T_e + T_d) - T_{br,3} \\ \frac{1}{2}(T_e - T_d) - T_{br,4} \end{bmatrix}. \tag{1}$$

As will be shown in section 3.2.3, it is beneficial to split the differential torque into a positive and negative

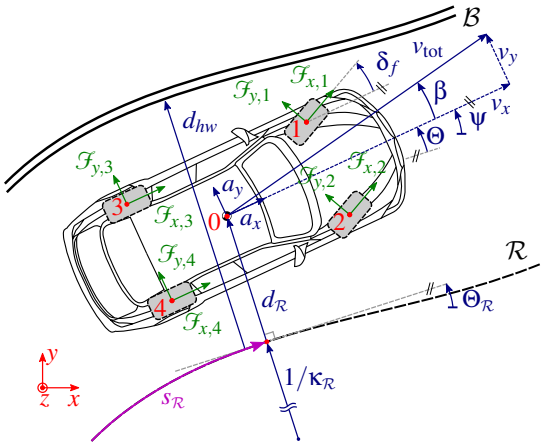

Figure 1: Top view of vehicle model on a racetrack with centre line $\mathcal{R}$ and track border $\mathcal{B}$ (Sedlacek 2020a).

part according to

$$T_d \coloneqq T_d^+ + T_d^- . \tag{2}$$

The total torque and total brake torque are computed by

$$T_{\text{tot}} = \sum_{k=1}^{4} T_k \quad \text{and} \quad T_{br,\text{tot}} = \sum_{k=1}^{4} T_{br,k}, \tag{3}$$

respectively. Furthermore, we assume $\delta_1 = \delta_f = \delta_2$ and $\delta_3 \equiv 0 \equiv \delta_4$. The $n_u = 8$ system inputs are accumulated in the input vector

$$\mathbf{u}^T = \begin{bmatrix} T_e & T_d^+ & T_d^- & \mathbf{T}_{br}^T & \delta_f \end{bmatrix} \in \mathbb{R}^{n_u} \tag{4a}$$

$$\text{with} \quad \mathbf{T}_{br}^T = \begin{bmatrix} T_{br,1} & T_{br,2} & T_{br,3} & T_{br,4} \end{bmatrix}. \tag{4b}$$

The longitudinal and lateral vehicle speed at the COG in the body reference frame are denoted with v_x and v_y, respectively. The yaw rate of the vehicle and the rotational wheel speeds are represented by $\dot{\psi}$ and ω_k, respectively. The vehicle motion is described using wheel forces which are represented by $\mathbf{F}_k^b = \begin{bmatrix} F_{x,k} & F_{y,k} \end{bmatrix}^T$ and $\mathcal{F}_k^w = \begin{bmatrix} \mathcal{F}_{x,k} & \mathcal{F}_{y,k} \end{bmatrix}^T$ in the body and the corresponding wheel coordinate frame, respectively. The wheel forces depend on the wheel loads and wheel slips, as specified in the appendix. The longitudinal drag force $F_{\text{air},x}$ and the rolling resistance torque $\mathcal{T}_{\text{roll},y,k}$ are given by (36) and (37), respectively. In the subsequent equations, we use following parameters: vehicle mass m, vehicle inertia J_{zz}, distance from COG to front axle l_f or to rear axle l_r, track width of front axle b_f or rear axle b_r, dynamic rolling radius of the corresponding tire r_k and inertia of the corresponding wheel-unit J_k. Applying Newton's second law (Schramm et al., 2014) provides equations for the translational motion

$$\begin{bmatrix} \dot{v}_x \\ \dot{v}_y \end{bmatrix} = \frac{1}{m} \underbrace{\begin{bmatrix} \sum_{k=1}^{4} F_{x,k} + F_{\text{air},x} \\ \sum_{k=1}^{4} F_{y,k} \end{bmatrix}}_{\coloneqq \begin{bmatrix} F_x & F_y \end{bmatrix}^T} + \begin{bmatrix} \dot{\psi} v_y \\ -\dot{\psi} v_x \end{bmatrix} \tag{5a}$$

and the yaw movement of the vehicle

$$\ddot{\psi} = \frac{\Sigma_f l_f - \Sigma_r l_r + \Delta_f \frac{b_f}{2} + \Delta_r \frac{b_r}{2}}{J_{zz}} \tag{5b}$$

$$\Sigma_f \coloneqq F_{y,1} + F_{y,2} \;\text{ and }\; \Sigma_r \coloneqq F_{y,3} + F_{y,4} \tag{5c}$$

$$\Delta_f \coloneqq F_{x,2} - F_{x,1} \;\text{ and }\; \Delta_r \coloneqq F_{x,4} - F_{x,3} \tag{5d}$$

as well as for the rotational wheel motion

$$\dot{\omega}_k = \frac{1}{J_k} \left(T_k - \mathcal{F}_{x,k} r_k + \mathcal{T}_{\text{roll},y,k} \right) \;\; \forall k \in \mathbb{K}. \tag{5e}$$

For the modelling of the SLD, we define the wheel speed difference of the rear axle and the corresponding differential equation as

$$\omega_d = \omega_4 - \omega_3 \;\text{ and }\; \dot{\omega}_d = \dot{\omega}_4 - \dot{\omega}_3, \tag{5f}$$

respectively. In order to avoid an algebraic loop when computing the wheel loads via (38a), delayed accelerations, given in the body reference frame, are introduced using first-order lag elements with time constant τ_{acc}

$$\dot{a}_j = \frac{1}{\tau_{\text{acc}}} \left(\frac{1}{m} F_j - a_j \right) \quad \forall j \in \{x, y\}. \tag{5g}$$

These low-pass filters can be motivated by neglected chassis dynamics (Bianco et al., 2019) and the dynamic tire force generation (Sedlacek et al., 2020b).

The centre line of the racetrack is denoted with $\mathcal{R}$ and characterised by its curvature $\kappa_{\mathcal{R}}$ over the arc length $s_{\mathcal{R}}$. The track boundary $\mathcal{B}$ is described using the arc length-dependent track half-width d_{hw}. The connection between vehicle model and track is established via curvilinear coordinates using (Sharp et al., 2000)

$$\dot{s}_{\mathcal{R}} = \frac{v_x \cos(\Theta) - v_y \sin(\Theta)}{1 - d_{\mathcal{R}} \kappa_{\mathcal{R}}}, \tag{6a}$$

$$\dot{d}_{\mathcal{R}} = v_x \sin(\Theta) + v_y \cos(\Theta) \quad \text{and} \tag{6b}$$

$$\dot{\Theta} = \dot{\psi} - \kappa_{\mathcal{R}} \dot{s}_{\mathcal{R}}. \tag{6c}$$

The difference between vehicle orientation and tangent angle of the reference line $\Theta_{\mathcal{R}}$ is given by the tangent error angle $\Theta = \psi - \Theta_{\mathcal{R}}$. The lateral deviation $d_{\mathcal{R}}$ describes the normal distance of the tangent to the COG of the vehicle.

Using (5) and (6), the system behaviour is characterised by a continuous, input nonaffine, nonlinear differential equation system

$$\dot{\mathbf{x}} = \mathbf{f}(\mathbf{x}, \mathbf{u}, \mathbf{p}) \in \mathbb{R}^{12} \tag{7}$$

with the state vector

$$\mathbf{x} = \begin{bmatrix} \mathbf{x}_{\text{veh}} \\ \mathbf{x}_{\text{ref}} \end{bmatrix} \text{ with } \mathbf{x}_{\text{ref}}^T = \begin{bmatrix} s_{\mathcal{R}} & d_{\mathcal{R}} & \Theta \end{bmatrix}, \tag{8a}$$

$$\mathbf{x}_{\text{veh}}^T = \begin{bmatrix} v_x & v_y & \dot{\psi} & \omega^T & a_x & a_y \end{bmatrix} \tag{8b}$$

$$\text{and } \omega^T = \begin{bmatrix} \omega_1 & \omega_2 & \omega_3 & \omega_d \end{bmatrix}. \tag{8c}$$

Furthermore, the values of the model parameters $\mathbf{p}$ are given in table 2.

3 OPTIMAL CONTROL PROBLEM

In this section, we present the nonconvex OCP for completing a lap in minimum time using the model introduced in section 2. Before formulating the constraints and cost function of the OCP in sections 3.2 and 3.3, several preliminaries are outlined in section 3.1. Model approximations are introduced to provide smooth system behaviour and avoid singularities,

the free final time OCP is transformed into an OCP with fixed final arc length and the OCP is scaled to enhance convergence rate.

The OCP is transcribed via Hermite-Simpson collocation and posed using the domain-specific modelling language *JuMP* (Dunning et al., 2017) for mathematical optimisation embedded in the programming language *Julia*. The resulting nonlinear program is solved with *IPOPT* which uses a primal-dual interior-point strategy with a filter line-search and further features for performance enhancement (Wächter and Biegler, 2006). Forward Mode Automatic Differentiation is embedded in the *JuMP*-framework yielding the necessary gradients and Hessians in advance in machine precision.

3.1 Preliminaries

We adopt the smooth approximations introduced in (Sedlacek et al., 2020a) to provide a differentiable system for the computation of the derivatives. On the one hand, we smooth the longitudinal slips (42a) via

$$\lambda_{x,k} \approx \frac{\Delta_{v,k}}{\frac{1}{2}\left(\Sigma_{v,k} + \sqrt{\Delta_{v,k}^2 + \varepsilon_{\lambda,x}}\right)} \tag{9a}$$

$$\text{with } \Delta_{v,k} = \omega_k r_k - v_{x,k} \text{ and} \tag{9b}$$

$$\Sigma_{v,k} = \omega_k r_k + v_{x,k} \quad \forall k \in \mathbb{K}. \tag{9c}$$

On the other hand, the total slips in (43c) are replaced by

$$\lambda_k \approx \sqrt{\lambda_{n,x,k}^2 + \lambda_{n,y,k}^2 + \varepsilon_{\lambda,\text{tot}}} \quad \forall k \in \mathbb{K} \tag{9d}$$

which also eliminates the singularity in (43d).

Minimum-time OCPs have a free final time. To generate a fixed final arc length problem, we change the independent variable to the arc length of the reference line associating all inputs and states explicitly to the position on the racetrack (Perantoni and Limebeer, 2014). This transformation requires a scaling of the differential equation system according to

$$\mathbf{x}'(s_\mathcal{R}) = \frac{\partial \mathbf{x}}{\partial s_\mathcal{R}} = \dot{\mathbf{x}}\frac{1}{\dot{s}_\mathcal{R}} = \frac{1}{\dot{s}_\mathcal{R}}\mathbf{f} =: \tilde{\mathbf{f}}. \tag{10}$$

After the transformation, the elapsed time is retrieved by the differential equation

$$t'(s_\mathcal{R}) = \frac{\partial t}{\partial s_\mathcal{R}} = \frac{1}{\dot{s}_\mathcal{R}} \quad \text{with} \quad t(s_{\mathcal{R},0}) = 0. \tag{11}$$

With transformation (10) in mind, we exchange the independent variables in the state vector (8) resulting in

$$\tilde{\mathbf{x}}^T = \begin{bmatrix} \mathbf{x}_\text{veh}^T & t & d_\mathcal{R} & \Theta \end{bmatrix}. \tag{12}$$

The corresponding differential equation in (7) is replaced with (11) and the right-hand side of the differential equation system is adapted according to (10).

The OCP is scaled according to (Sedlacek et al., 2020a) to improve convergence speed. This includes adapting the states and inputs, which represent decision variables when collocation is used, to lie within the the range $[-1,1]$. Furthermore, constraints are normalised to the domain $[-1,0]$. The interrelations between the scaled and non-scaled variables are given by

$$\hat{\mathbf{x}} = \mathbf{S}_{\tilde{x}}\tilde{\mathbf{x}} + \mathbf{k}_{\tilde{x}} \;\Leftrightarrow\; \tilde{\mathbf{x}} = \mathbf{S}_{\tilde{x}}^{-1}(\hat{\mathbf{x}} - \mathbf{k}_{\tilde{x}}) \tag{13a}$$

$$\hat{\mathbf{u}} = \mathbf{S}_u\mathbf{u} + \mathbf{k}_u \;\Leftrightarrow\; \mathbf{u} = \mathbf{S}_u^{-1}(\hat{\mathbf{u}} - \mathbf{k}_u) \tag{13b}$$

$$\hat{\mathbf{f}}(\hat{\mathbf{x}},\hat{\mathbf{u}}) = \mathbf{S}_{\tilde{x}}\tilde{\mathbf{f}}(\hat{\mathbf{x}},\hat{\mathbf{u}}). \tag{13c}$$

Adequate values for the scaling matrices $\mathbf{S}_{\tilde{x}}$ and $\mathbf{S}_u$ as well as the shifting vectors $\mathbf{k}_{\tilde{x}}$ and $\mathbf{k}_u$ are given in (Sedlacek et al., 2020a).

3.2 Constraints

This section presents the constraints for the contemplated optimisation problem which are used to consider the system dynamics, set initial values, capture non-modelled physical effects and avoid numerical problems.

3.2.1 Collocation Constraints

We use Hermite-Simpson collocation to consider the continuous system dynamics (13c) in the OCP. Thus, the system inputs and the right-hand sides of the differential equations are approximated by piecewise quadratic polynomials. The integration interval $s_\mathcal{R} \in [s_{\mathcal{R},0}, s_{\mathcal{R},f}]$ is divided into n_seg segments with $n_\text{coll} = n_\text{seg} + 1$ collocation points. Simpson quadrature is applied on each segment $i = 0,\ldots,n_\text{seg}-1$ yielding the collocation constraints

$$\hat{\mathbf{x}}_{i+1} - \hat{\mathbf{x}}_i = \frac{h_i}{6}(\hat{\mathbf{f}}_i + 4\hat{\mathbf{f}}_{i+\frac{1}{2}} + \hat{\mathbf{f}}_{i+1}) \tag{14a}$$

$$\hat{\mathbf{x}}_{i+\frac{1}{2}} = \frac{1}{2}(\hat{\mathbf{x}}_i + \hat{\mathbf{x}}_{i+1}) + \frac{h_i}{8}(\hat{\mathbf{f}}_i - \hat{\mathbf{f}}_{i+1}) \tag{14b}$$

with the segment width $h_i = s_{\mathcal{R},i+1} - s_{\mathcal{R},i}$ (Betts, 2010; Kelly, 2017). The margins of each segment represent collocation points with the corresponding values $(\cdot)_i$ and $(\cdot)_{i+1}$. Values at the midpoint are marked as $(\cdot)_{i+\frac{1}{2}}$. All following constraints, except for the initial conditions, are set at each collocation point and midpoint but we omit the index for readability. Once the optimal values at the collocation points and midpoints are computed, the intermediate values for the inputs and states are determined by piecewise quadratic and

piecewise cubic polynomials, respectively. The corresponding formulas can be found in (Sedlacek et al., 2020a).

3.2.2 Initial Values

The vehicle starts at the centre of the racetrack in alignment with the reference line yielding $d_{\mathcal{R}} = \Theta = \psi = 0$. The first track section is straight, thus lateral speed, yaw rate and initial steering angles are set to zero. By setting the initial longitudinal speed to a small value $v_x = v_{x,k} = 1\frac{m}{s}$, we avoid the singularity of the tire slip angles (42b) at vanishing speed. We presume that the vehicle is initially in steady-state, no brake torque is applied, the SLD is open and aerodynamic forces are compensated by the rear tire forces. Thus, accelerations are zero resulting in only static wheel loads. Then, (5a) and (5e) enable the computation of the front and rear tire forces as well as the engine torque according to (Sedlacek et al., 2020b)

$$\mathcal{F}_{x,1} = \frac{1}{r_1}\mathcal{T}_{\text{roll},y,1} = \mathcal{F}_{x,2}, \tag{15a}$$

$$\mathcal{F}_{x,3} = \frac{1}{2}(-F_{\text{air},x} - \mathcal{F}_{x,1} - \mathcal{F}_{x,2}) = \mathcal{F}_{x,4}, \tag{15b}$$

$$T_e = \mathcal{F}_{x,3} r_3 + \mathcal{F}_{x,4} r_4 - \mathcal{T}_{\text{roll},y,3} - \mathcal{T}_{\text{roll},y,4}. \tag{15c}$$

Using the tire forces (15a)-(15b), the longitudinal slip can be computed from (43f) and the initial rotational wheel speeds can be identified via (42a).

3.2.3 Input Constraints

Due to actuator limitations, box constraints are set for the brake torques

$$0 \leq T_{br,k} \leq \overline{T}_{br,k} \quad \forall k \in \mathbb{K} \tag{16}$$

as well as for the front steering angle

$$-\overline{\delta}_f \leq \delta_k \leq \overline{\delta}_f \quad \forall k \in \{1,2\}. \tag{17}$$

The wheel-based engine torque depends on the engine characteristic as well as the gear ratios and efficiencies of transmission and SLD. Since we assume a rigid connection between engine and rear axle, the torque constraint is formulated utilising the rotational speed of the rear axle

$$\omega_r \approx \frac{1}{2}(\omega_3 + \omega_4). \tag{18}$$

Assuming constant mechanical efficiencies and an automatic selection of the optimal gear, the admissible set for the wheel-based engine torque T_e is approximated by the constraints

$$0 \leq T_e \leq \overline{T}_e \text{ and } T_e \leq \frac{\overline{P}_e}{\omega_r} =: T_{e,\text{pow}} \tag{19a}$$

using the maximum engine torque $\overline{T}_e$ and maximum engine power $\overline{P}_e$ (Sedlacek et al., 2020b; Gillespie, 1992). We presume that the vehicle has a launch control functionality which immediately provides the maximum torque $\overline{T}_e$ at the race start. Thus, the combined constraint

$$T_{e,\text{con}} := \min(\overline{T}_e, T_{e,\text{pow}}) \tag{20}$$

represents the upper boundary for the engine torque.

3.2.4 Semi-activity Constraint

Semi-active components do not introduce energy into systems and thus fulfill the passivity constraint (Savaresi et al., 2010). In this section, we present a novel convexification procedure for semi-active components which have a convex subset in each of the two quadrants dictated by the passivity premise. The approach is depicted using the SLD as an example, whereas we compare our method with previous approaches.

The SLD enables a lateral distribution of torque, however the direction of the torque transfer depends on the rotational speed difference ω_d within the SLD. As mentioned in section 1, previous approaches have modelled the differential torque via

$$T_d = \xi_d \omega_d \tag{21}$$

or a more complicated version with trigonometric functions. If T_d and ξ_d are chosen as system inputs, the SLD can be included into the OCP using the constraints

$$T_d = \xi_d \omega_d \tag{22a}$$

$$-\overline{T}_d \leq T_d \leq \overline{T}_d \tag{22b}$$

$$-T_e \leq T_d \leq T_e \tag{22c}$$

with $\overline{T}_d$ denoting the maximum differential torque of the SLD. With ξ_d and ω_d being an input and state,

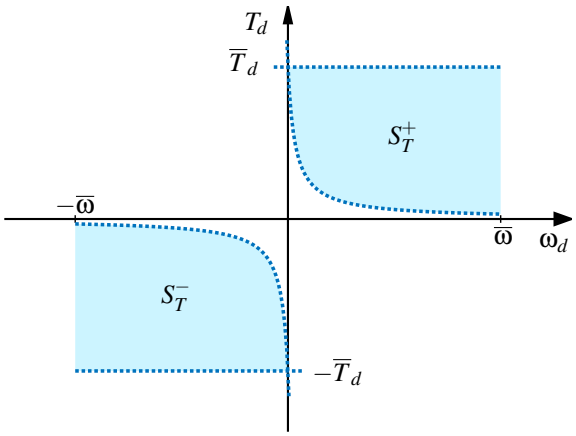

Figure 2: Convexified set for SLD (exaggerated).

both represent optimisation variables. Thus, equality constraint (22a) is quadratic in the optimisation parameters and would prevent a convex OCP beforehand (Boyd and Vandenberghe, 2004).

Alternatively, (21) can be inserted into the differential equations with ξ_d being a system input. However, this would result in the nonconvex sets

$$-\overline{T}_d \leq \xi_d \omega_d \leq \overline{T}_d \tag{23a}$$
$$-T_e \leq \xi_d \omega_d \leq T_e. \tag{23b}$$

In this paper, we suggest splitting the differential torque T_d into a positive part T_d^+ and a negative one T_d^- which enables the formulation of the convex sets

$$-T_e \leq T_d^+ + T_d^- \leq T_e \tag{24a}$$
$$S_T^+ := \{(T_d^+, \omega_d) | T_d^+ \in \left]0, \overline{T}_d\right] \wedge g_T^+ \leq 0\} \tag{24b}$$
$$\text{with } g_T^+ := -T_d^+ \left(\omega_d + \frac{\varepsilon_\mathrm{T}}{\overline{T}_d}\right) + \varepsilon_\mathrm{T} \tag{24c}$$
$$S_T^- := \{(T_d^-, \omega_d) | T_d^- \in \left[-\overline{T}_d, 0\right[\wedge g_T^- \leq 0\} \tag{24d}$$
$$\text{with } g_T^- := -T_d^- \left(\omega_d - \frac{\varepsilon_\mathrm{T}}{\overline{T}_d}\right) + \varepsilon_\mathrm{T}. \tag{24e}$$

Figure 2 depicts sets (24b) and (24d). Being confined to the first and third quadrant, the passivity constraint is satisfied. By selecting a sufficiently small parameter $\varepsilon_\mathrm{T} = 10^{-10}$, the excluded area for simultaneously small wheel speed differences ω_d and small differential torques T_d is negligible. Notice that with (24b)-(24e) from $\omega_d = 0$ follows $T_d^+ = \overline{T}_d = -T_d^-$ which results in $T_d = 0$. However, we point out that this convexification comes at the price of a larger OCP due to one extra input and additional constraints.

Theorem 1. *The set given by* (24) *is convex.*

Proof. Convexity of set (24) is proven using theorems from (Boyd and Vandenberghe, 2004). Set (24a) represents a half-space which is convex. We denote the graph associated with the epigraph (24c) by

$$f(T_d^+) := \frac{\varepsilon_\mathrm{T}}{T_d^+} - \frac{\varepsilon_\mathrm{T}}{\overline{T}_d}. \tag{25a}$$

The second derivative of (25a)

$$f''(T_d^+) = \frac{2\varepsilon_\mathrm{T}}{T_d^{+3}} > 0 \;\; \forall T_d^+ > 0 \tag{25b}$$

is positive for the parameter range $T_d^+ \in \mathbb{T}^+ := \left]0, \overline{T}_d\right]$ given in (24b). Thus, the graph is convex in this region and consequently (24c) represents a convex set for $T_d^+ \in \mathbb{T}^+$. Furthermore, the box constraint $T_d^+ \in \mathbb{T}^+$ in (24b) defines a polyhedron which is also convex. The intersection of convex sets results in a convex set. Thus, set (24b) is convex. The convexity proof of (24d) is equivalent, since sets (24b) and (24d) are established analogously. Finally, the intersection of the convex sets (24a), (24b) and (24d) yields a convex set. □

Remark 1. *It is tempting to choose the set*

$$S_T^+ := \{(T_d^+, \omega_d) | T_d^+ \in \left[0, \overline{T}_d\right] \wedge T_d^+ \omega_d \geq 0\}.$$

However, this set is nonconvex since it includes arbitrary ω_d, such as $\omega_d = -c < 0$, if $T_d^+ = 0$. If we exclude $T_d^+ = 0$ by choosing the convex set

$$S_T^+ := \{(T_d^+, \omega_d) | T_d^+ \in \left]0, \overline{T}_d\right] \wedge T_d^+ \omega_d \geq 0\},$$

we still cannot guarantee that $T_d = 0 \forall \omega_d = 0$.

Remark 2. *The presented approach is applicable to other semi-active actuators with convex subsets in the first and third quadrant. Considering semi-active dampers with damper speed v_d, a possible convex set can be approximated by splitting the damper force according to $F_d = F_d^+ + F_d^-$ and using the constraints*

$$\underline{k}_d v_d \leq F_d^+ \leq \bar{k}_d v_d \;\text{ and }\; F_d^+ \leq \hat{k}_{d,0} + \hat{k}_{d,1} v_d$$

with analogous constraints for F_d^-. Therein we use coefficients $\underline{k}_d$ and $\bar{k}_d$ to restrict the admissible area yielding $F_d^+(v_d = 0) = 0$ and employ an upper boundary using a linear constraint with parameters $\hat{k}_{d,0}$ and $\hat{k}_{d,1}$. Note that by using different constraint parameters for F_d^+ and F_d^-, differing characteristics for compression and rebound can be implemented without discarding smoothness of the OCP. Other convex subsets for semi-active dampers are depicted in (Savaresi et al., 2010).

3.2.5 State Constraints

Since driving backwards is not expedient on racetracks, positive longitudinal speeds and wheel speeds are enforced by the box constraints

$$0 < \underline{v}_x \leq v_x \leq \bar{v}_x \quad \text{and} \quad 0 \leq \omega_k \leq \overline{\omega} \; \forall k \in \mathbb{K}. \tag{26}$$

The yaw rate and steering angles are generally small enough, especially on racetracks, that (26) results in $v_{x,k}, v_{x,k} > 0$ (Sedlacek et al., 2020b). This enables the simplification made in (42a) and avoids the singularity in (42b).

In order to keep the vehicle on the racetrack, the path constraints

$$-d_{hw} + \frac{b_\mathrm{veh}}{2} \leq d_\mathcal{R} \leq d_{hw} - \frac{b_\mathrm{veh}}{2} \tag{27}$$

limit the lateral deviation of the vehicle employing the arc length-dependent track half-width d_{hw} and chassis width b_veh.

For an efficient tire usage, we restrict the tire

forces (43) to stay within the region of adhesion which excludes sliding and thus decreases tire wear. Since tire wear reduces the tire force potential, this constraint is eligible. This is accomplished by the load-dependent friction ellipse constraints for the tire slips

$$\left(\frac{\lambda_{x,k}}{\lambda^{\star}_{x,k}}\right)^2+\left(\frac{\lambda_{y,k}}{\lambda^{\star}_{y,k}}\right)^2-1\leq 0\ \ \forall k\in\mathbb{K} \tag{28}$$

using (42a), (42b) and (44b) (Sedlacek et al., 2020b). When wheels lift off, no tire force can be generated. To avoid introducing additional discontinuities as in (Perantoni and Limebeer, 2014) and since the lift-off of wheels is undesired for industrial sports cars, we enforce positive wheel loads (38a) with

$$F_{z,k}>0\quad\forall k\in\mathbb{K}. \tag{29}$$

Furthermore, the additional constraint

$$\dot{s}_{\mathcal{R}}\geq\varepsilon_{\dot{s}}>0 \tag{30}$$

is employed to avoid dividing by zero when using the transformation (10). Since we exclude driving backwards, this assumption is legitimate.

3.3 Objective

The cost function is comprised of three objectives according to

$$J=J_t+J_{\dot{u}}+J_{\eta}. \tag{31}$$

The main goal is minimising the required lap time which is accomplished with

$$J_t=\int_{t_0}^{t_f}1dt=\int_{s_{\mathcal{R},0}}^{s_{\mathcal{R},f}}\frac{1}{\dot{s}_{\mathcal{R}}}ds_{\mathcal{R}}=t(s_{\mathcal{R},f}). \tag{32}$$

To avoid non-unique solutions and therefore improve convergence, a small regularisation term which is quadratic in the inputs can be added to the objective function (Kelly, 2017). Using Simpson quadrature and the input derivative vector $\hat{\mathbf{u}}'(s_{\mathcal{R}})$, we include the regularisation term

$$J_{\dot{u}}=\varepsilon_{\dot{u}}\sum_{j=1}^{n_u}\sum_{i=0}^{n_{seg}-1}\frac{h_i}{6}j_{\dot{u},ji} \tag{33a}$$

$$j_{\dot{u},ji}=\hat{u}'_j(s_{\mathcal{R},i})^2+4\,\hat{u}'_j\left(s_{\mathcal{R},i}+\frac{h_i}{2}\right)^2+\hat{u}'_j(s_{\mathcal{R},i}+h_i)^2 \tag{33b}$$

which generates a preference for smooth input solutions. Smooth inputs are generally desirable for human drivers which justifies the penalty term (33a). The computation of the input derivatives is shown in (Sedlacek et al., 2020a).

To enhance efficiency and durability, simultaneous drive and brake torques are avoided by adding the objective (Sedlacek et al., 2020b)

$$J_{\eta}=\frac{\varepsilon_{\eta}}{T_{\text{norm}}}\sum_{i=0}^{n_{\text{seg}}-1}\frac{h_i}{6}j_{\eta,i} \tag{34a}$$

$$j_{\eta,i}=T_{\eta}(s_{\mathcal{R},i})+4\,T_{\eta}\left(s_{\mathcal{R},i}+\frac{h_i}{2}\right)+T_{\eta}(s_{\mathcal{R},i}+h_i) \tag{34b}$$

$$T_{\eta}(s_{\mathcal{R},i})=T_e(s_{\mathcal{R},i})T_{br,\text{tot}}(s_{\mathcal{R},i}) \tag{34c}$$

$$T_{\text{norm}}=\overline{T}_e+\overline{T}_{br,r}. \tag{34d}$$

The unscaled torques are used in (34c), since they are limited to positive values. Scaling factors $\varepsilon_{\dot{u}}$ and ε_{η} are chosen sufficiently small so that the modified objective (31) is nearly time-optimal.

4 RESULTS

The OCP presented in section 3 is solved using a discretisation mesh of 1000 equally spaced collocation points yielding a mesh interval of about 2.5 metres. The optimal trajectories for the vehicle with an open differential at the rear axle instead of the SLD, which we name setup C0, have been computed in (Sedlacek et al., 2020b). Configuration C1 represents a vehicle with SLD at the rear axle and $\overline{T}_d=1250$Nm. Using (38b), we define the torque shift variable as

$$k_d:=-\frac{T_d}{F_{z,0,r}}\ \text{ with }\ F_{z,0,r}=\rho_1\,l_f\,g\,r_3. \tag{35}$$

It represents the lateral torque shift of the SLD normalised by the static rear axle load. The torque shift variable (35) is displayed in figure 3 together with the acceleration and braking points which are characterised by sign changes in T_{tot}. The first subplot of figure 4 illustrates the track curvature and the lap time advantage progression Δt of C1. The wheel speed difference and differential torque for C1 are shown in the second subplot. The third subplot considers setup C1 and depicts the individual wheel torques, the total torque and the upper boundary for the engine torque (20).

As expected, acceleration starts at the corner apexes and high speed corners like ① and ③ are passed without braking. The lateral wheel load shift during cornering results in different optimal slips (44b) between the left and right wheel of an axle. Thus, the SLD enhances traction conditions during cornering by applying a higher drive torque to the outer wheel at the expense of a lower drive torque at the inner wheel. Only small torques are transmitted

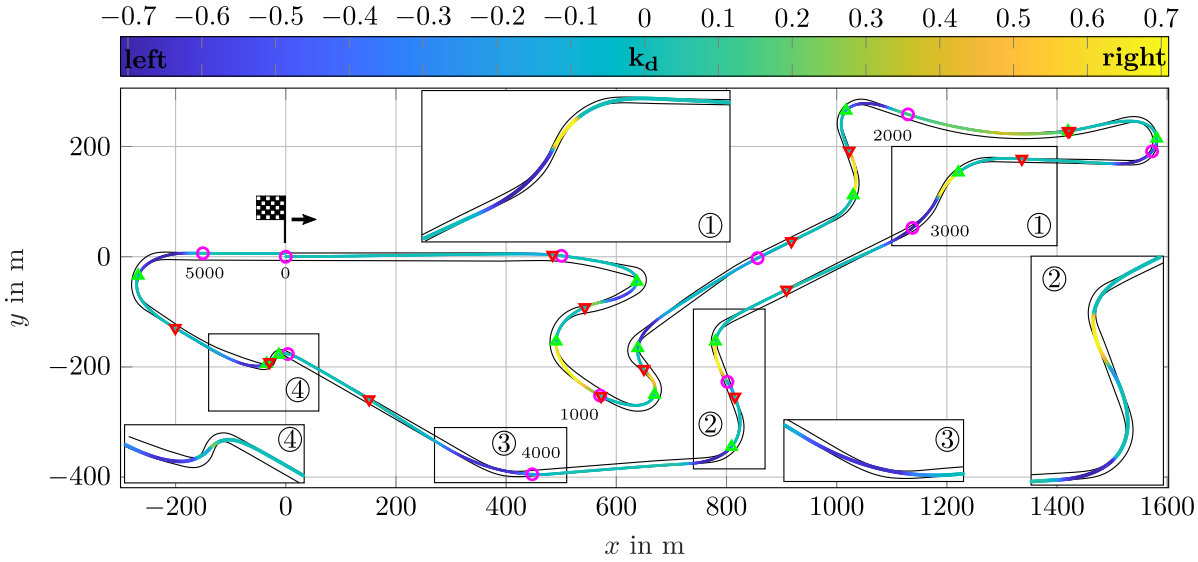

Figure 3: Normalised torque shift variable for lateral drive torque distribution via SLD at the rear axle with $\overline{T}_d = 1250$ Nm. Symbols: ○ 500m marks, △ start acceleration, ▽ start braking.

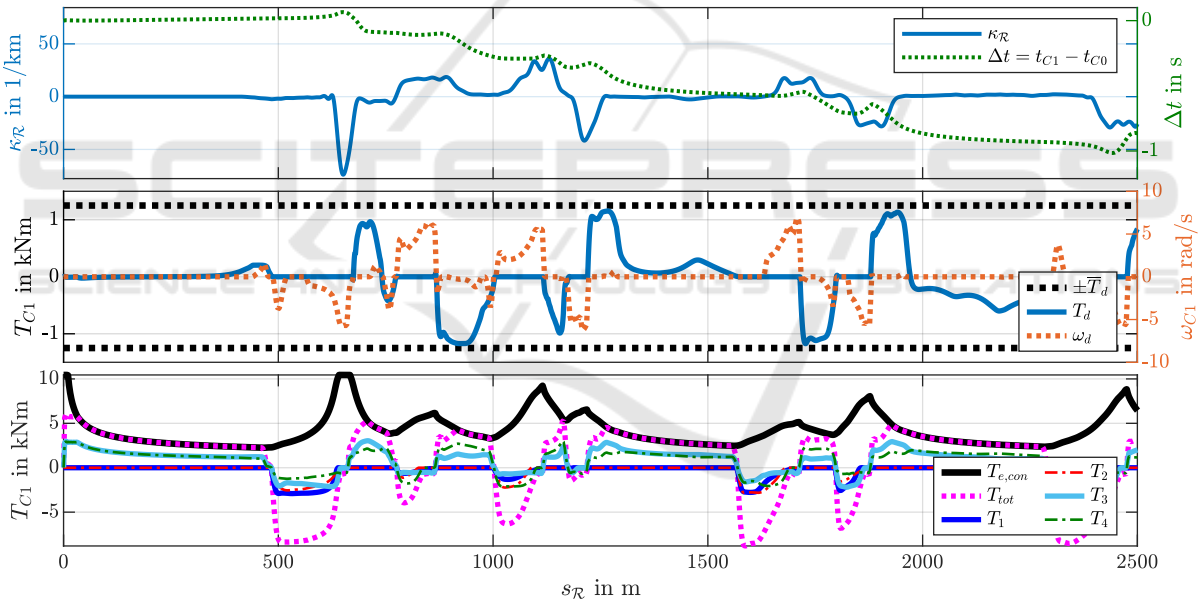

Figure 4: Track curvature, progression of lap time benefit, wheel speed difference and torques.

by the SLD when driving on paths with small curvature and no differential torque is applied during braking due to (24a) and (34a). The lateral torque distribution, either by the SLD or the braking system, affects the yaw motion of the vehicle: An additional yaw momentum is generated by the difference in longitudinal tire forces between the left and right side. When accelerating after corner apexes, the lateral drive torque allocation by the SLD increases agility, whereas a stabilising momentum is induced by the braking system before corners. The lateral drive torque distribution by the SLD is primarily performed after corner apexes to enhance acceleration and agility. With a lap time of 146.68 seconds, an overall improvement of 2.37 seconds or 1.59% is achieved, whereas lap time benefits due to the SLD occur primarily when exiting corners.

The lap time sensitivity regarding the maximum torque of the SLD is depicted in figure 5. The sensitivity curve is constructed via cubic spline interpolation of computed sampling points which are generated by solving the OCP for several values of $\overline{T}_d$. Gener-

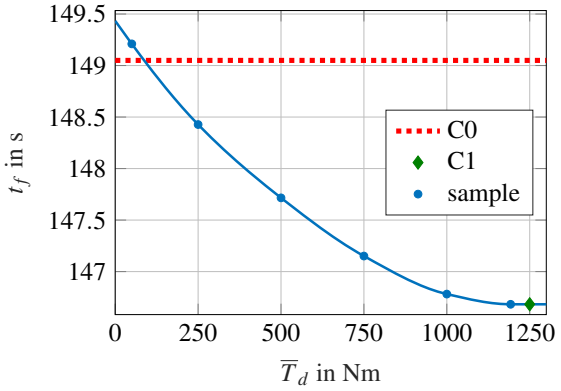

Figure 5: Lap time over maximum torque of SLD.

ally, the increased vehicle weight and inertia due to the SLD, implemented according to (Sedlacek et al., 2020b), is detrimental for cornering. The benefit of lateral drive torque allocation outweighs this disadvantage for $\overline{T}_d > 87.3$Nm, whereas lap time reduces with increasing $\overline{T}_d$. Since for the current track and vehicle setup $|T_d| \leq 1193$Nm holds, lap time reductions due to the SLD only occur up this threshold value. However, this result strongly depends on the considered track and vehicle setup.

5 CONCLUDING REMARKS

A novel OCP-modelling approach for a broad class of semi-active actuators has been presented. The procedure transforms the originally nonconvex set dictated by the passivity constraint into multiple convex sets. However, this convexification requires an extra input and generally a higher number of constraints. The method has been applied to compute minimum-lap-time trajectories for a vehicle with rear-wheel drive and SLD at the rear axle. The OCP has been solved using Hermite-Simpson collocation implemented in an open-source framework. Compared to a vehicle with open differential instead of the SLD, lap time is greatly reduced by 2.37 seconds or 1.59% with lap time benefits primarily occurring when exiting corners. Although the overall OCP remains nonconvex for the considered application, the presented convexification measure is a first step towards a fully convex OCP for such vehicles which we will address in the future. Considering our previous work (Sedlacek et al., 2020b; Sedlacek et al., 2020a), the proposed method will be used to compare different powertrain topologies for vehicles with combustion engine or electric machines while simultaneously identifying the respective optimal passive vehicle setups. A detailed experimental comparison of the proposed modelling-method with the existing methods presented in section 3.2.4 is subject of future work.

REFERENCES

Betts, J. T. (2010). *Practical Methods for Optimal Control and Estimation Using Nonlinear Programming*. Society for Industrial and Applied Mathematics, second edition.

Bianco, N. D., Bertolazzi, E., Biral, F., and Massaro, M. (2019). Comparison of direct and indirect methods for minimum lap time optimal control problems. *Vehicle System Dynamics*, 57(5):665–696.

Boyd, S. and Vandenberghe, L. (2004). *Convex Optimization*. Cambridge University Press, Cambridge, seventh edition.

Cheli, F., Pedrinelli, M., Resta, F., Travaglio, G., Zanchetta, M., and Zorzutti, A. (2006). Development of a new control strategy for a semi-active differential for a high-performance vehicle. *Vehicle System Dynamics*, 44(sup1):202–215.

Dunning, I., Huchette, J., and Lubin, M. (2017). Jump: A modeling language for mathematical optimization. *SIAM Review*, 59(2):295–320.

Gillespie, T. (1992). *Fundamentals of Vehicle Dynamics*. SAE International.

Kelly, D. (2008). *Lap time simulation with transient vehicle and tyre dynamics*. PhD thesis, Cranfield University.

Kelly, M. (2017). An introduction to trajectory optimization: How to do your own direct collocation. *SIAM Review*, 59(4):849–904.

Kim, Y., Kwon, C., Moon, H., Kim, K., Cho, J., and Kong, K. (2018). Optimization of semi-active pneumatic actuators for an exoskeleton robot for running. *2018 15th International Conference on Ubiquitous Robots (UR)*, pages 119–124.

Krüger, W. (2000). *Integrated design process for the development of semi-active landing gears for transport aircraft*. PhD thesis, University of Stuttgart.

Limebeer, D., Perantoni, G., and Rao, A. (2014). Optimal control of formula one car energy recovery systems. *International Journal of Control*, 87(10):2065–2080.

Limebeer, D. J. N. and Perantoni, G. (2015). Optimal control of a formula one car on a three-dimensional track-part 2: Optimal control. *Journal of Dynamic Systems, Measurement, and Control*, 137(5).

Perantoni, G. and Limebeer, D. J. (2014). Optimal control for a formula one car with variable parameters. *Vehicle System Dynamics*, 52(5):653–678.

Poussot-Vassal, C., Savaresi, S. M., Spelta, C., Sename, O., and Dugard, L. (2010). A methodology for optimal semi-active suspension systems performance evaluation. In *49th IEEE Conference on Decision and Control (CDC)*, pages 2892–2897.

Savaresi, S. M., Poussot-Vassal, C., Spelta, C., Sename, O., and Dugard, L. (2010). *Semi-Active Suspension Control Design for Vehicles*. Elsevier, first edition.

Schramm, D., Hiller, M., and Bardini, R. (2014). *Vehicle Dynamics - Modeling and Simulation*. Springer, Berlin, Heidelberg.

Sedlacek, T., Odenthal, D., and Wollherr, D. (2020a). Minimum-time optimal control for battery electric vehicles with four wheel-independent drives considering electrical overloading. *Vehicle System Dynamics*, Submitted for publication.

Sedlacek, T., Odenthal, D., and Wollherr, D. (2020b). Minimum-time optimal control for vehicles with active rear-axle steering, transfer case and variable parameters. *Vehicle System Dynamics*, pages 1–29.

Sharp, R., Casanova, D., and Symonds, P. (2000). A mathematical model for driver steering control, with design, tuning and performance results. *Vehicle System Dynamics*, 33(5):289–326.

Tremlett, A., Massaro, M., Purdy, D., Velenis, E., Assadian, F., Moore, A., and Halley, M. (2015). Optimal control of motorsport differentials. *Vehicle System Dynamics*, 53(12):1772–1794.

Tremlett, A. J. and Limebeer, D. J. N. (2016). Optimal tyre usage for a formula one car. *Vehicle System Dynamics*, 54(10):1448–1473.

Wächter, A. and Biegler, L. T. (2006). On the implementation of an interior-point filter line-search algorithm for large-scale nonlinear programming. *Math. Program.*, 106(1):25–57.

APPENDIX

Subsequently, further modelling details are addressed. We assume windless conditions and consider the longitudinal drag force (Schramm et al., 2014)

$$F_{\text{air},x} = -\frac{1}{2}\,\rho_{\text{air}}\,c_{\text{air},x}A_{\text{air}}\,v_x\,\sqrt{v_x^2+v_y^2}. \tag{36}$$

The parameters are air density ρ_{air}, drag coefficient $c_{\text{air},x}$ and vehicle crossspan area A_{air}. Due to rolling resistance forces, the tires are subject to load-dependent torques opposed to the rolling direction

$$\mathcal{T}_{\text{roll},y,k} = -f_{\text{roll},0}\,F_{z,k}\,r_k \tag{37}$$

with the rolling resistance coefficient $f_{\text{roll},0}$.
For simplicity, quasi steady-state conditions are presumed for the wheel load computation. Assuming that the roll momentum is allocated via the roll moment distribution factor ξ_{roll}, the wheel loads are computed via (Sedlacek et al., 2020b)

$$\begin{bmatrix}F_{z,1}\\F_{z,2}\\F_{z,3}\\F_{z,4}\end{bmatrix} = \rho_1\begin{bmatrix}l_r\,g-h\,a_x\\l_r\,g-h\,a_x\\l_f\,g+h\,a_x\\l_f\,g+h\,a_x\end{bmatrix} + \rho_2\begin{bmatrix}\frac{-\xi_{\text{roll}}}{b_f}\\\frac{\xi_{\text{roll}}}{b_f}\\\frac{\xi_{\text{roll}}-1}{b_r}\\\frac{1-\xi_{\text{roll}}}{b_r}\end{bmatrix} \tag{38a}$$

$$\text{with}\quad \rho_1 = \frac{m}{2(l_f+l_r)}\quad\text{and}\quad \rho_2 = m\,h\,a_y. \tag{38b}$$

The velocity of the wheel centre points in the body coordinate frame is denoted with $\mathbf{v}_k^b = \begin{bmatrix}v_{x,k} & v_{y,k}\end{bmatrix}^T\ \forall k\in\mathbb{K}$ and computed by

$$\mathbf{v}_1^b = \begin{bmatrix}v_x-\dot{\psi}\frac{b_f}{2}\\v_y+\dot{\psi}l_f\end{bmatrix},\quad \mathbf{v}_2^b = \begin{bmatrix}v_x+\dot{\psi}\frac{b_f}{2}\\v_y+\dot{\psi}l_f\end{bmatrix}, \tag{39a}$$

$$\mathbf{v}_3^b = \begin{bmatrix}v_x-\dot{\psi}\frac{b_r}{2}\\v_y-\dot{\psi}l_r\end{bmatrix}\quad\text{and}\quad \mathbf{v}_4^b = \begin{bmatrix}v_x+\dot{\psi}\frac{b_r}{2}\\v_y-\dot{\psi}l_r\end{bmatrix}. \tag{39b}$$

These speeds are transformed into the corresponding wheel coordinate frame via

$$\mathbf{v}_k^w = \begin{bmatrix}v_{x,k}\\v_{y,k}\end{bmatrix} = \mathbf{R}_z(\delta_k)\begin{bmatrix}v_{x,k}\\v_{y,k}\end{bmatrix}\ \forall k\in\mathbb{K}. \tag{40}$$

Therein the two-dimensional rotation matrix

$$\mathbf{R}_z(\gamma) \coloneqq \begin{bmatrix}\cos(\gamma) & \sin(\gamma)\\-\sin(\gamma) & \cos(\gamma)\end{bmatrix} \tag{41}$$

performs a mathematical rotation by the angle γ around the z-axis of the inertial frame. Assuming $\omega_k, v_{x,k}\geq 0\ \forall k\in\mathbb{K}$, the longitudinal wheel slips are defined as

$$\lambda_{x,k} = \frac{\omega_k r_k - v_{x,k}}{\max\left(\omega_k r_k, v_{x,k}\right)}. \tag{42a}$$

The wheel slip angles are given by

$$\lambda_{y,k} = \delta_k - \arctan\left(\frac{v_{y,k}}{v_{x,k}}\right). \tag{42b}$$

We employ the tire model presented in (Sedlacek et al., 2020b) which is based on (Kelly, 2008). For readability, we only list the basic equations for the longitudinal tire forces and omit the index k. Equations for the lateral tire forces are constructed analogously. The tire parameters differ in the longitudinal and lateral direction as well as for the front and rear wheels. The linear equations

$$\lambda_{\max,x} = \frac{\bar{\lambda}_{b,x}-\bar{\lambda}_{a,x}}{\bar{F}_b-\bar{F}_a}\left(F_z-\bar{F}_a\right)+\bar{\lambda}_{a,x} \tag{43a}$$

$$D_x = \frac{\bar{D}_{b,x}-\bar{D}_{a,x}}{\bar{F}_b-\bar{F}_a}\left(F_z-\bar{F}_a\right)+\bar{D}_{a,x} \tag{43b}$$

approximate the load-dependent tire slip optimum and the nonlinear wheel load degressivity, respectively. The variables in (43a) and (43b) marked as $\bar{(\cdot)}$ represent fixed tire parameters. The normalised slips and the combined slip coefficient are defined as

$$\lambda_{n,x} = \frac{\lambda_x}{\lambda_{\max,x}}\quad\text{and}\quad \lambda = \sqrt{\lambda_{n,x}^2+\lambda_{n,y}^2}, \tag{43c}$$

respectively. Using the tire shape parameter C_x, the tire force shape curve is characterised by

$$\mathcal{F}_{\text{shape},x} = \frac{\lambda_{n,x}}{\lambda}\sin\left(C_x\arctan(B_x\lambda)\right) \tag{43d}$$

$$\text{with}\quad B_x = \frac{\pi}{2\arctan(C_x)}. \tag{43e}$$

With (38a), (43b), (43d) and the road friction coefficient μ, the longitudinal component of the tire force is given by

$$\mathcal{F}_x = \mu F_z D_x \mathcal{F}_{\text{shape},x}. \tag{43f}$$

The total tire force $\mathcal{F}^w = \begin{bmatrix}\mathcal{F}_x & \mathcal{F}_y\end{bmatrix}$ reaches its peak values at the friction limit which can be represented by the ellipse equation

$$\left(\frac{\lambda_x}{\lambda_x^\star}\right)^2 + \left(\frac{\lambda_y}{\lambda_y^\star}\right)^2 = 1. \tag{44a}$$

The positive optimum slip values are given by

$$\lambda_x^\star = \frac{\tan\left(\frac{\pi}{2C_x}\right)\left((F_z - \bar{F}_a)\bar{\lambda}_{b,x} - (F_z - \bar{F}_b)\bar{\lambda}_{a,x}\right)}{B_x(\bar{F}_b - \bar{F}_a)}. \tag{44b}$$

With $\mathcal{F}_k^w \ \forall k \in \mathbb{K}$ denoting the tire force vector in the corresponding wheel coordinate frame, the tire force components in the body reference frame are given by

$$\mathbf{F}_k^b = \mathbf{R}_z(-\delta_k)\mathcal{F}_k^w \quad \forall k \in \mathbb{K}. \tag{45}$$

Parameter values for the considered OCP and the vehicle model are listed in table 1 and 2, respectively.

Table 1: Parameter values for OCP.

	variable	value
optimisation	$\overline{T}_{br,1/2}/\overline{T}_{br,3/4}$	7024 Nm/4032 Nm
	$\overline{T}_e/\overline{P}_e$	10.5 kNm/390.6 kW
	$\overline{\delta}_f$	0.6981 rad
	$\underline{v}_x/\overline{v}_x$	0.9 ms^{-1}/83.3 ms^{-1}
	$\overline{\omega}$	277.8 rad/s
	$\varepsilon_{\dot{u}}/\varepsilon_\eta$	$2\cdot10^{-2}/2\cdot10^{-4}$
	$\varepsilon_{\dot{s}}$	1.0 ms^{-1}
	$\varepsilon_{\lambda,x}/\varepsilon_{\lambda,\text{tot}}$	$10^{-6}/10^{-8}$

Table 2: Parameter values for model.

	variable	value
env.	g	9.81 ms^{-2}
	μ	1.0
	ρ_{air}	1.2041 kgm^{-3}
tires	$\bar{F}_a/\bar{F}_b$	2000 N/6000 N
	$\bar{\lambda}_{a,x,1/2}/\bar{\lambda}_{b,x,1/2}$	0.124/0.108
	$\bar{\lambda}_{a,y,1/2}/\bar{\lambda}_{b,y,1/2}$	0.144/0.133
	$\bar{D}_{a,x,1/2}/\bar{D}_{b,x,1/2}$	1.560/1.396
	$\bar{D}_{a,y,1/2}/\bar{D}_{b,y,1/2}$	1.603/1.258
	$C_{x,1/2}/C_{y,1/2}$	1.949/1.941
	$\bar{\lambda}_{a,x,3/4}/\bar{\lambda}_{b,x,3/4}$	0.111/0.099
	$\bar{\lambda}_{a,y,3/4}/\bar{\lambda}_{b,y,3/4}$	0.109/0.099
	$\bar{D}_{a,x,3/4}/\bar{D}_{b,x,3/4}$	1.898/1.597
	$\bar{D}_{a,y,3/4}/\bar{D}_{b,y,3/4}$	1.945/1.515
	$C_{x,3/4}/C_{y,3/4}$	1.949/1.858
vehicle	$r_{1/2}/r_{3/4}$	0.3429 m/0.3474 m
	$b_f/b_r/b_{\text{veh}}$	1.626 m/1.594 m/1.90 m
	$l_f/l_r/h$	1.479 m/1.503 m/0.540 m
	m/J_{zz}	1988 kg/3485 kgm^2
	$J_{1/2}/J_{3/4}$	2.20 kgm^2/6.95 kgm^2
	A_{air}	2.44 m^2
	$c_{\text{air},x}/f_{\text{roll},0}$	0.31/0.0031
	τ_{acc}	0.03 s

SCITEPRESS SCIENCE AND TECHNOLOGY PUBLICATIONS